

Article

Fluorescent Detection of Carbon Disulfide by a Highly Emissive and Robust Isoreticular Series of Zr-Based Luminescent Metal Organic Frameworks (LMOFs)

Ever Velasco^{1,†}, Yuki Osumi^{1,†}, Simon J. Teat², Stephanie Jensen³, Kui Tan⁴, Timo Thonhauser³ and Jing Li^{1,*} 

¹ Department of Chemistry and Chemical Biology, Rutgers University, 123 Bevier Road, Piscataway, NJ 08854, USA; eov2@chem.rutgers.edu (E.V.); yto1@scarletmail.rutgers.edu (Y.O.)

² Advanced Light Source Lawrence Berkeley National Laboratory, Berkeley, CA 94720, USA; sjteat@lbl.gov

³ Department of Physics and Center for Functional Materials, Wake Forest University, Winston-Salem, NC 27109, USA; jensensj@wfu.edu (S.J.); thonhauser@wfu.edu (T.T.)

⁴ Department of Materials Science & Engineering, University of Texas at Dallas, Richardson, TX 75080, USA; kuitan@utdallas.edu

* Correspondence: jingli@rutgers.edu

† These authors contributed equally to this work.

Abstract: Carbon disulfide (CS₂) is a highly volatile neurotoxic species. It is known to cause atherosclerosis and coronary artery disease and contributes significantly to sulfur-based pollutants. Therefore, effective detection and capture of carbon disulfide represents an important aspect of research efforts for the protection of human and environmental health. In this study, we report the synthesis and characterization of two strongly luminescent and robust isoreticular metal organic frameworks (MOFs) Zr₆(μ₃-O)₄(OH)₈(tcbpe)₂(H₂O)₄ (here termed **1**) and Zr₆(μ₃-O)₄(OH)₈(tcbpe-f)₂(H₂O)₄ (here termed **2**) and their use as fluorescent sensors for the detection of carbon disulfide. Both MOFs demonstrate a calorimetric bathochromic shift in the optical bandgap and strong luminescence quenching upon exposure to carbon disulfide. The interactions between carbon disulfide and the frameworks are analyzed by in-situ infrared spectroscopy and computational modelling by density functional theory. These results reveal that both the Zr metal node and organic ligand act as the preferential binding sites and interact strongly with carbon disulfide.

Keywords: metal organic frameworks (MOFs); coordination polymers (CP); luminescent sensing; carbon disulfide



Citation: Velasco, E.; Osumi, Y.; Teat, S.J.; Jensen, S.; Tan, K.; Thonhauser, T.; Li, J. Fluorescent Detection of Carbon Disulfide by a Highly Emissive and Robust Isoreticular Series of Zr-Based Luminescent Metal Organic Frameworks (LMOFs). *Chemistry* **2021**, *3*, 327–337. <https://doi.org/10.3390/chemistry3010024>

Received: 23 December 2020

Accepted: 17 February 2021

Published: 1 March 2021

Publisher's Note: MDPI stays neutral with regard to jurisdictional claims in published maps and institutional affiliations.



Copyright: © 2021 by the authors. Licensee MDPI, Basel, Switzerland. This article is an open access article distributed under the terms and conditions of the Creative Commons Attribution (CC BY) license (<https://creativecommons.org/licenses/by/4.0/>).

1. Introduction

Metal organic frameworks (MOFs) are an extremely versatile class of crystalline, permanently porous inorganic-organic materials that have gained significant attention over the past two decades. These materials are constructed from the self-assembly process of metal ions or metal clusters and organic linkers to form coordinatively bonded extended and porous network structures. The ability to control the nature of the metal ions and linkers make MOFs a promising class of materials for applications in gas storage and separation, catalysis, luminescent sensing, and other areas [1–9].

The incorporation of either luminescent metal nodes or organic linkers into frameworks make it possible to design and construct luminescent MOFs (LMOFs). As a subcategory of MOFs, LMOFs have been extensively studied for the luminescent detection of chemical species, as LED phosphors, and so on [10–16]. As chemical sensors, they serve as promising candidates for the detection of a wide range of molecules whereby analyte interactions alter the optical properties of the LMOF. These changes in their optical properties may manifest as either quenching or enhancement in luminescence intensity, and/or shifts in emission energy. Such effects are governed by electron or energy transfer processes that occur between the analyte and the framework [5,17]. LMOF-based sensors

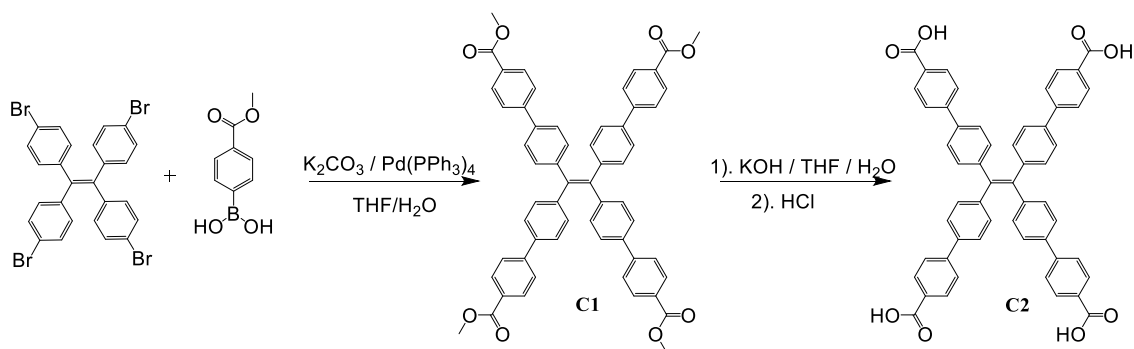
offer rapid and sensitive detection limits resulting in a promising and simple alternative for current sensing technology that requires the use of expensive instrumentation.

Carbon disulfide (CS₂) is a highly volatile neurotoxic species produced in the manufacturing of viscose rayon fibers, the production of agricultural pesticides, as a vulcanizing accelerant, and as a chemical by-product of syngas produced from biomass [18–20]. CS₂ is a nonpolar organic solvent that can dissolve a wide range of chemicals; however, it is also known to cause atherosclerosis and coronary artery disease [21]. In addition to its detrimental effects on human health, environmentally, CS₂ is known to contribute significantly to sulfur-based pollutants as it readily oxidizes into carbonyl sulphide and sulfur dioxide that contribute to the formation of acid rain [22]. Despite the toxicity of CS₂ there has been limited work on the luminescent detection of CS₂ and less for the capture of this chemical using MOFs [23]. While MOFs have been reported previously for the luminescent sensing of CS₂, they are limited to magnesium, indium, calcium, and lead-based coordination polymers which often suffer from framework instability [24–27]. In addition, the exact interactions between the frameworks and CS₂ were not investigated in depth in these studies. To the best of our knowledge, the current work represents the first example that makes use of highly robust zirconium-based MOFs for the detection of CS₂. Our study is not only on the luminescent sensing performance of the two Zr-LMOFs but also on the molecular interactions that occur in the MOF-analyte system with the help of in-situ Fourier-transform infrared (FTIR) spectroscopic experiments and density functional theory (DFT) calculations.

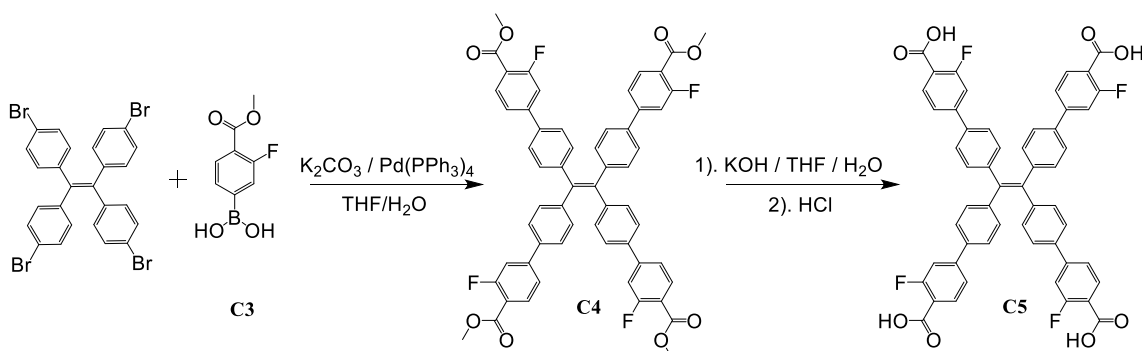
2. Materials and Methods

2.1. Materials

All reagents were used directly from commercially available sources without further purification. Both ligands were synthesized according to previously published methods with slight variations [28,29]. Their synthesis is outlined in Schemes 1 and 2, and detailed in the Supporting Information.



Scheme 1. Synthesis of H₄tcbpe.



Scheme 2. Synthesis of H₄-tcbpe-F.

2.2. Synthesis of 1 and 2

$\text{Zr}_6(\mu_3\text{-O})_4(\text{OH})_8(\text{tcbpe})_2(\text{H}_2\text{O})_4$ (here termed **1**). A solution containing 35.7 mg of $\text{ZrOCl}_2 \cdot x\text{H}_2\text{O}$ was suspended in 3 mL of DMA, to which 1.7 mL of formic acid was added and sonicated for 10 min until fully dissolved. To this solution was added 16.7 mg of H_4tcbpe and it was sonicated for an additional 10 min. The suspension was then placed in a pre-heated 120 °C oven for 48 h. Reactions were filtered to afford (20 mg 53.1% yield based on the inorganic salt of) pale green needle-shaped crystals suitable for single crystal X-ray diffraction.

$\text{Zr}_6(\mu_3\text{-O})_4(\text{OH})_8(\text{tcbpe-f})_2(\text{H}_2\text{O})_4$ (here termed **2**). Similarly, 35.7 mg of $\text{ZrOCl}_2 \cdot x\text{H}_2\text{O}$, 3 mL of DMA, and 1.7 mL of formic acid were added into a 20 mL scintillation vial and sonicated until dissolved. Upon full dissolution, 18.5 mg of $\text{H}_4\text{tcbpe-F}$ was added into the vial and it was sonicated for 10 min. The cloudy suspension was placed into a preheated oven at 120 °C for 48 h. Pale green needle-shaped single crystals were collected after filtration (20 mg, 52% yield based on the inorganic salt).

2.3. Powder X-ray Diffraction (PXRD)

Powder X-ray diffraction measurements were taken at room temperature from 3–35° (2 θ) with a scan speed of 2° min⁻¹ using a copper k α radiation source ($\lambda = 1.5406 \text{ \AA}$) from a Rigaku Ultima-IV X-ray diffractometer (Billerica, MA, USA).

2.4. Thermogravimetric Analysis (TGA)

The thermal decomposition analysis was performed using a TA instruments Q5000IR analyzer (TA Instruments, New Castle, DE, USA) under a flow of nitrogen and sample purge rate at 10 mL/min and 12 mL/min, respectively. About 10 mg of sample was loaded on the platinum pan and gradually increased from room temperature to 600 °C with a heating rate of 10 °C min⁻¹.

2.5. Diffuse Reflectance Measurement(UV-VIS)

Absorption spectra at room temperature were collected with a Shimadzu UV-3600 (Kyoto, Japan) from 200–800 nm. Samples were prepared by evenly loading the powders in between two quartz glass plates. The collected reflectance data were then converted through the Kubelka–Munk function, $\alpha/S = (1 - R)^2/2R$ (α is absorption coefficient, S is scattering coefficient, and R is reflectance).

2.6. Photoluminescence Spectra (PL)

Photoluminescence data were recorded at room temperature using a Duetta fluorescence and absorbance spectrometer from Horiba scientific (Kyoto, Japan). Fluorescence measurements of single crystals of **1** or **2** were collected at different states. Since **1** and **2** undergo mechanochromic shifts in emission that resemble those of outgassed samples, the fluorescence spectra were collected in both the as-made and outgassed states. To collect fluorescent measurements for as-made samples, reactions were filtered off, washed with DMF and immediately measured. Outgassed samples were dried prior to treatment with the specified solvent exchanged measurements without grinding.

2.7. Internal Quantum Yield Measurements (QY)

Internal quantum yield measurements were measured on a C9920-02 absolute quantum yield system from Hamamatsu Photonics (Shizuoka, Japan). The light source is a 150 W xenon monochromatic with a 3.3 inch integrating sphere. Either sodium salicylate (360 nm excitation) or cerium-doped yttrium aluminum garnet (YAG:Ce, 450 nm excitation) were used as standards for QY measurements with QY values of 60% and 95% at their respective wavelengths.

2.8. Chemical Stability Experiments

The chemical stability of **1** and **2** was explored: in brief, approximately 20 mg of **1** or **2** was immersed into 10 mL of different solutions of varying pH and allowed to set for 48 h. Samples were collected through vacuum filtration, washed with 3 aliquots of water (20 mL) and 3 aliquots of *N,N'*-Dimethylformamide (10 mL). After washing, samples were collected and used to collect PXRD patterns.

2.9. Fluorescent Sensing Experiments

Fluorescent measurements for the detection of CS₂ were performed using 5 mg of **1** and **2** previously ground in an agate mortar and pestle with 2 mL of DMF. The resulting slurry was then pipetted into a cuvette. Grinding in DMF allows for the formation of fine powder without affecting the luminescence profile of the as-made samples (mechanochromic behavior if ground dry, Figure S19). The PL spectra of the outgassed samples may be replicated after extensive grinding. Under continuous stirring, CS₂ was added in and allowed to stir for 5 min in between sample measurements of increasing concentration of CS₂.

2.10. In-Situ Infrared Spectroscopy (FTIR)

In-situ IR measurements were performed on a Nicolet 6700 FTIR spectrometer (Waltham, MA, USA) using a liquid N₂-cooled mercury cadmium telluride (MCT-A) detector. A vacuum cell is placed in the sample compartment of the infrared spectrometer with the sample at the focal point of the beam. The samples (~5 mg) were gently pressed onto KBr pellets and placed into a cell that was connected to a vacuum line for evacuation. The samples of **1** and **2** were activated by evacuation overnight at 150 °C, respectively, and then cooled back to room temperature for CS₂ vapor exposure measurement.

2.11. Computational Methods

We explored the interactions of the CS₂ with the LMOFs by looking at the charge rearrangement upon binding of the CS₂ by subtracting CS₂ and framework charge densities from the CS₂ + framework charge density. This allowed us to see how the guest molecules rearranged the charge density of the system. The charge densities were obtained by first calculating the optimized structures in the Vienna Ab initio Simulation Package (VASP) [30,31] at the DFT level with the vdW-DF exchange-correlation functional [32–34] in order to capture the long range van der Waals interactions between the CS₂ and the framework. Optimizations were performed until SCF loops reached an energy convergence of 1×10^{-4} eV and forces were below 1 meV/Å for each atom. Only the Γ -point was considered with a plane-wave energy cutoff of 600 eV. Once the optimizations were completed, the charge density images were created using the aforementioned methods.

3. Results and Discussion

Here, we report the synthesis of Zr₆(μ₃-O)₄(OH)₈(tcbpe)₂(H₂O)₄ (**1**) and Zr₆(μ₃-O)₄(OH)₈(tcbpe-F)₂(H₂O)₄ (**2**) through modified conditions [35] using ZrOCl₂·xH₂O, H₄tcbpe (or H₄tcbpe-F), DMA (*N,N'*-dimethylacetamide) and formic acid at 120 °C for 48 h. Compound **1** crystallizes in an orthorhombic crystal system, space group *Cmcm* with Zr₆O₄(OH)₈(H₂O)₄ secondary-building units (SBUs) that are bridged together by 4-connected organic linkers. The overall structure is a two-fold interpenetrated network with *scu* topology (Figure 1a–d). Single crystals for **2** were not solved but the PXRD patterns of as-made **1**, as-made **2**, and the simulated diffraction pattern of **1** are in good agreement, suggesting it is isorecticular to **1** (Figure 2a). Both compounds inherit flexibility from their interpenetrated network where the nature of the solvent within the pores can alter the structure slightly. Compound **1** was previously reported under packing with solvents such as DMF, EtOH, Et₂O, MeOH, and toluene; here we include the single crystal structure for the altered packing with DMA molecules within the pores (CCDC: 2005129). The chemical stability of **1** and **2** in water and acidic/basic aqueous solutions at room temperature was

confirmed by PXRD analysis (Figure 2b and Figure S1, Electronic Supporting Information (ESI)). The thermal stability of the two compounds was evaluated by thermogravimetric (TG) analysis. Both compounds remained highly crystalline upon heating at 150 and 200 °C for 6 h, as confirmed by PXRD patterns (Figures S2 and S3).

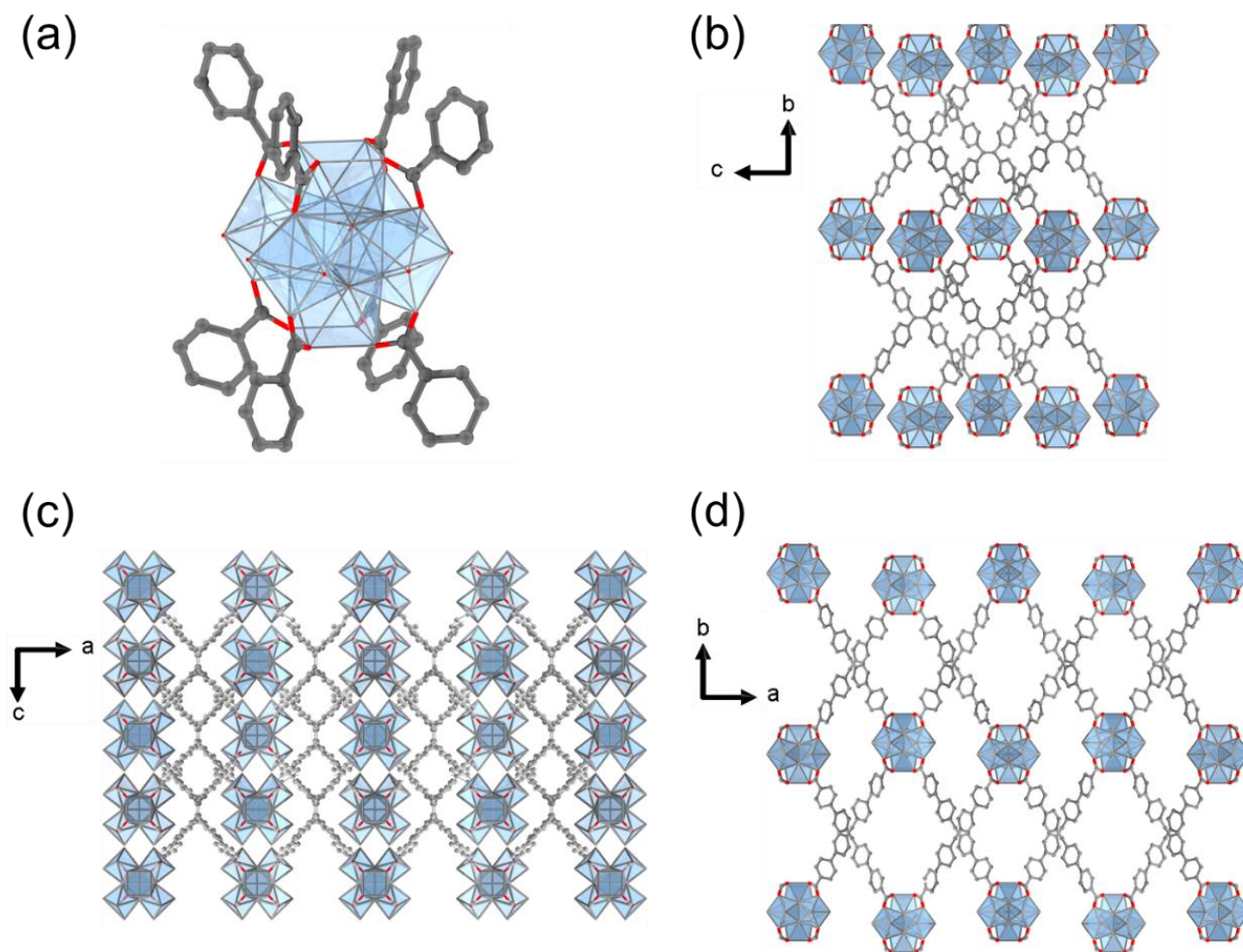


Figure 1. Crystal structure of **1**. (a) 8-connected zirconium SBU, (b) two-fold interpenetrated nets along the crystallographic *a*-axis, (c) *b*-axis, and (d) *c*-axis.

As demonstrated in previous work, the incorporation of a strongly emissive ligand with aggregation induced-emission (AIE) properties into a framework results in highly emissive LMOFs [28,29,36–38]. The optical properties of **1** and **2** were analyzed by UV-Vis and photoluminescence (PL) spectroscopy. Under the excitation of UV light (365 nm) **1** has an emission centered at 457 nm (blue color) with a relatively high internal quantum yield (IQY) of 68%. Upon outgassing, **1** undergoes a bathochromic shift and emits at 532 nm (green color) under 455 nm excitation (Figure S4, ESI). An IQY value of 69% is achieved. Similarly, the as-made sample of **2** exhibits an emission peak centered at 492 nm under 365 nm excitation and an IQY value of 48.7%. Upon fully outgassing, **2** displays an emission centered at 557 nm under 455 nm excitation with a significantly increased IQY value of 73.6% (Figure S5, ESI). The emission profiles of the individual ligands used in the assembly of **1** and **2** resemble the emission profiles of the outgassed versions of both materials (Figure S6, ESI). The observed shift in emission of **1** and **2** corresponds well with their optical band gap shifts from 2.72 eV to 2.44 eV (Figure S7, ESI) and from 2.53 eV to 2.42 eV (Figure S8, ESI) in the as-made and outgassed samples, respectively. To outgas samples and retain permanent porosity we referred to a previously published

technique that exploits the use of organic solvents with low dipole moments and surface tension due to the structural sensitivity upon outgassing [39]. Briefly, samples were solvent exchanged with dimethylformamide, dichloromethane and finally hexane without letting samples dry in between steps. Small amounts of samples were removed and studied by TGA to ensure complete removal of solvents in between solvent exchange steps (Figure S10, ESI). Using this solvent exchange strategy, N₂ isotherms collected at 77 K indicate that **1** has a Brunauer-Emmett-Teller (BET) surface area of ~527 m²/g with a pore size of ~6 Å (Figure S11, ESI). The pore size distribution analysis suggests that **1** is microporous, with a pore diameter of ~5.8 Å. Furthermore, the flexible nature of the framework is seen as the structure undergoes significant peak shifting upon outgassing, and this flexible nature will be explained later (Figure S12, ESI). Both **1** and **2** are stable in either aqueous, acidic, or high boiling point solvents which prompted us to study their sensing performance under these solvent systems. Upon the addition of CS₂ to **1** and **2** we noted the following changes: i) significant decrease in luminescence intensity; ii) large bathochromic shift in the optical band gap; iii) slight structural alternations upon packing of CS₂ that manifest as shift in peaks of their respective PXRD patterns. Subsequent photoluminescence studies reveal that **1** and **2** are good sensors for the detection of CS₂. The addition of CS₂ at various concentrations to suspensions of **1** (Figure 2c) in DMA led to gradual decrease in the overall luminescent intensity associated with a color change (Figure 2e,f). We then tested the quenching efficiency of **1** and **2** in low concentrations of CS₂ (in the range of 0 to 350 μM, Figures S13 and S14, ESI). From this information we applied a Stern–Volmer analysis (Figures S15 and S16, ESI), where we observed a linear decrease in luminescence intensity with regards to the concentration of analyte. From the Stern–Volmer plots, we calculated the limit of detection (LOD) for **1** and **2** (based on 3σ/m) to be 2.89 ppm and 2.58 ppm, respectively. As seen in Figure 2d and Figure S9, ESI, **1** and **2** exhibit a significant reduction in optical bandgap associated with color change upon exposure to CS₂. As-made samples of **1** and **2** possess band gaps of 2.72 eV and 2.53 eV that shift to 2.38 eV and 2.36 eV, respectively. To understand the PL quenching mechanism, we investigated the possibility of both energy transfer and electron transfer processes. The optical absorption spectrum of CS₂ and the emission profiles of **1** and **2** show no spectral overlap (Figure 3a and Figure S17, ESI), clearly suggesting that there is essentially no energy transfer [40]. The quenching is likely due to the electron transfer as described in detail in our previous studies [40–43]. Previous work has demonstrated that the highest occupied molecular orbital (HOMO) and lowest unoccupied molecular orbital (LUMO) energy levels of a LMOF can be altered through the functionalization of the organic linker [44] which can improve the efficiency of the electron transfer process. In this study, we selected fluorine for the ligand functionalization as the process can be carried out by Suzuki cross coupling, and as it is small enough not to cause a severe steric effect resulting in a different structure [45]. Indeed, the overall connectivity and topology of the resulting MOF was retained thus generating an isorecticular structure. However, the results from our sensing experiments suggest that fluorine functionalization did not provide a noticeable improvement to the overall quenching performance. To demonstrate the selectivity of the MOF, we also tested the change in luminescence of sample **1** when suspended in other common volatile organic compounds (VOCs) including dichloromethane, ethyl acetate, acetone, methanol, benzene, and toluene. In all cases, very little quenching was observed (Figure S20).

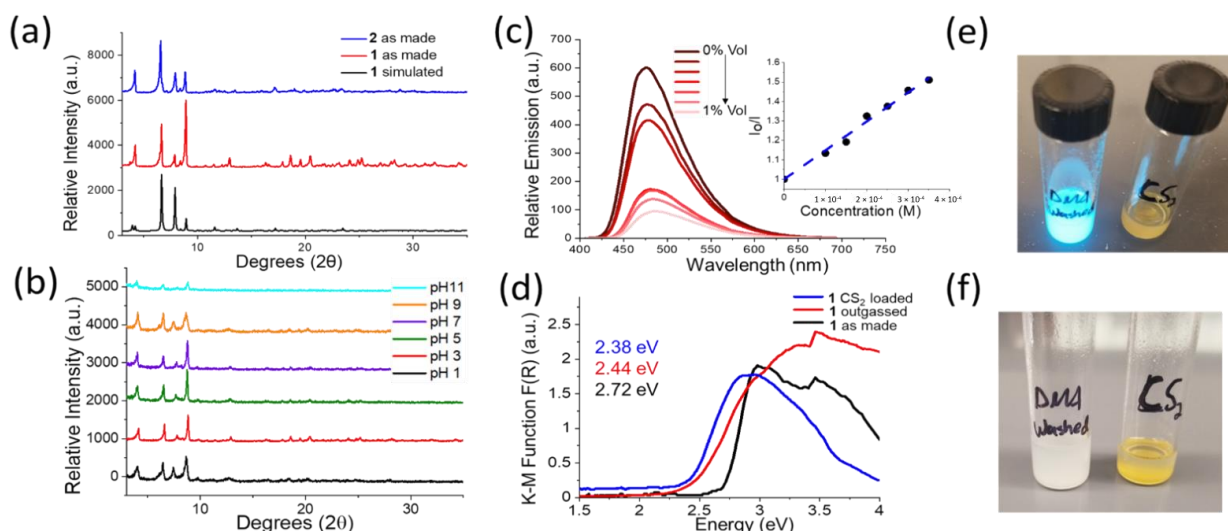


Figure 2. (a) PXRD patterns of simulated **1** compared to the experimental patterns of **1** and **2**. (b) PXRD patterns of **1** after exposure to different pH values. (c) Luminescence quenching profile of **1** when exposed to increasing concentrations of CS₂ in DMA (inset: the Stern–Volmer plot). (d) Optical band gaps of **1** in different forms. A shift in optical band gap of **1** after exposure to CS₂ was observed. (e,f) Images of **1** before and after exposure to CS₂: under UV excitation (e) and under daylight (f).

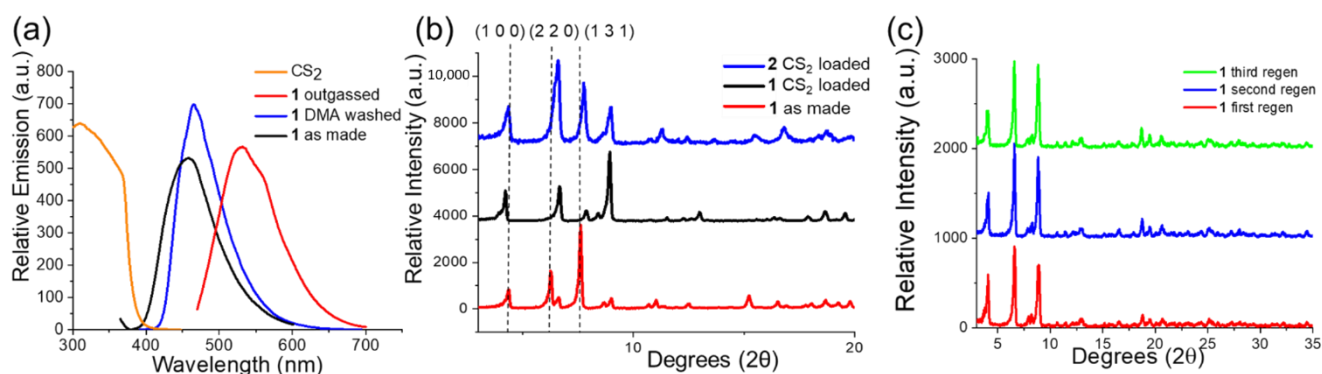


Figure 3. (a) The optical absorption spectrum of pure CS₂ and emission spectra of **1** in different forms (as-made, DMA washed and outgassed). (b) PXRD patterns of the as-made **1** and CS₂-loaded **1** and **2**. (c) The PXRD patterns of **1** after three cycles of regeneration upon exposure to CS₂, 1 M HCl, and DMF.

In addition, PXRD analysis on both **1** and **2** recovered after exposure to CS₂ indicates structural changes related to the packing of the interpenetrated nets as the shifts in the diffraction peaks correspond mainly to the (2 2 0) and (1 3 1) planes (Figure 3b). The PXRD patterns of the as-made samples of **1** and **2** are nearly identical with no obvious shifts in the peak positions, suggesting that, even with the addition of the fluorine atom to the organic linker, the packing of the interpenetrated nets remains the same and that the shifting between the two nets is a direct result from the loading of CS₂. Exposing CS₂-loaded samples of **1** to dilute HCl reverts the structures to their original as-made form with respect to both structural and luminescent profiles, and samples maintain their crystallinity for up to three cycles (Figure 3c). To understand the analyte interactions that occur within the framework at the molecular level and identify potential interaction sites within the system we used in-situ IR spectroscopy to probe the interaction of **1** and **2** upon exposure of CS₂ in the vapor phase. The IR measurements were conducted to monitor changes in the vibrational modes of **1** or **2** before and after exposure to 3 Torr of CS₂.

The spectra were collected in-situ during the exposure to CS₂ and desorption under evacuation of gas phase. Carbon dioxide, a close relative to CS₂, is known to interact strongly with Zr-MOFs through the Zr metal nodes. [46] The spectroscopic results here on CS₂ also reveal that the molecule has a prominent interaction with bridged μ_3 -OH bonds from the Zr₆ SBU. In addition, it also interacts with the C-H bonds of the organic linkers in both **1** and **2** (Figure 4a and Figure S18, ESI), as evidenced by following observations. First, upon exposure to CS₂, the vibrational bands of both **1** and **2** at 3674 cm⁻¹, corresponding to stretching modes $\nu(\mu_3\text{-OH})$ of the Zr₆ node [47], show an obvious red shift in the difference spectra (Figure 4a). Furthermore, the in plane and out of plane C-H vibrational modes of the organic linkers at 1200–600 cm⁻¹ are significantly perturbed. In addition to these changes in the vibrational bands of **1** and **2**, the spectra of adsorbed CS₂ collected under desorption also show notable differences with respect to those of free CS₂ (Figure 4a and Figure S17, ESI). Specifically, the hot band ($\nu_1 + \nu_3$) exhibits a much sharper peak centered at 2164 cm⁻¹ [48]. As seen in the desorption profiles, the application of a static vacuum is capable of desorbing CS₂ from the framework, indicative of a relatively weak interaction. Thus, the in-situ IR study not only confirms the interaction of CS₂ with the framework but also reveals that the hydrogen atoms of the ligand may play a role in the binding of CS₂. To help elucidate the interactions between CS₂ and the MOF we also employed DFT calculations to analyze the electronic structure of CS₂-loaded **1**. Within the structure of **1**, there are two distinct types of “pockets” near the Zr-SBU where the interactions between CS₂ and the framework may occur. As seen in Figure 4b, pocket I sits between two of the coordinately saturated sites occupied by two organic ligands where Zr-O-C bonds predominate, and pocket II sits between two Zr atoms and contains two hydroxyl functional groups where Zr-O-H bonds predominate. The charge rearrangement diagram shows a significant increase in electron density near the zirconium node (Figure 4c) at an isolevel of 2×10^{-4} eV/Å, which indicates a weak bond. It reveals an electron density contribution from CS₂ onto the Zr atom, the oxygen atoms directly bonded to Zr, and the hydrogen atoms of the linker closest to that site. However, it is important to note that the most preferential binding interaction of CS₂ and the framework occurs in pocket II where the Zr-O-C bonds predominate. While the in-situ IR measurements reveal that there is a shift in the vibrational modes of the Zr-OH bond of pocket I, the computational calculations find pocket II to be a more favorable binding site. The sulfur atom binds in a head-on fashion and the zirconium node experiences a significant loss in electron density with a calculated binding energy between 300–500 meV. However, it would be feasible to assume that exposure to excess CS₂ will first occupy all the most preferential binding sites and then occupy the remaining Zr-OH bonds of SBU within the framework, which explains the observed IR shift.

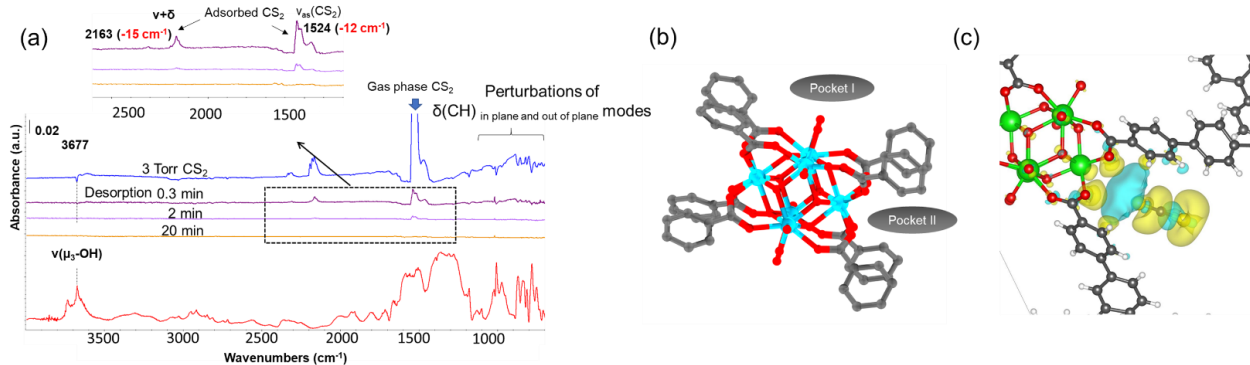


Figure 4. (a) difference IR spectra of **1** during adsorption (~3 min, top) and desorption (middle three) of CS₂, referenced to activated MOF in vacuum (bottom). The CS₂ gas signal of asymmetric stretching band ν_3 at 1560–1400 cm⁻¹ is not fully shown due to its prohibitively high intensity. (b) The two distinct pockets in the MOF structure that are surrounded by Zr-O bonds. (c) Charge rearrangement diagram showing an increase in electron density (yellow) and loss of electron density (cyan) upon CS₂ interaction at an isolevel of 2×10^{-4} eV.

4. Conclusions

In conclusion, we have synthesized and characterized two robust and isoreticular Zr-based LMOFs with underlying *scu* topology and two-fold interpenetration. Both **1** and **2** are strongly emissive with high PL quantum yields of 68% (69%) and 49% (74%), respectively in as-made (outgassed) form. Investigation of their use as fluorescent sensors for the detection of CS₂ shows that both compounds exhibit a bathochromic shift in their optical absorption spectra and significantly reduced emission intensity upon exposure to CS₂. Luminescent sensing experiments reveal that both are capable of sensing CS₂ in solutions of DMA with detection limits of 2.89 ppm and 2.58 ppm, respectively. Upon adsorption of CS₂, subtle shifts in the PXRD patterns imply that the packing of the two interpenetrated nets is altered. To confirm the molecular interactions occurring between CS₂ and the framework, in-situ IR experiments were performed upon exposure to CS₂. These results confirm that CS₂ interacts with the OH- groups from the Zr-SBU and the C-H groups from the organic linker. DFT calculations further corroborate this conclusion and suggest that the preferential binding sites for CS₂ occur closest to the oxygen atoms from the carboxylic acid group that coordinates directly to the Zr-SBU. This work provides another example where luminescence-based sensing can be achieved via host-guest interactions that occur between the analyte and Zr-based MOFs. Our work demonstrates a new host-guest interaction that may be useful for the future development of highly sensitive MOF materials capable of sensing CS₂ in the vapor phase.

Supplementary Materials: The following are available online <https://www.mdpi.com/2624-8549/3/1/24/s1>. CCDC 2005129 contains the supplementary crystallographic data for this manuscript. This data may be obtained free of charge via www.ccdc.cam.ac.uk/data_request/cif, by emailing data_request@ccdc.cam.ac.uk, or by contacting The Cambridge Crystallographic Data Centre, 12 Union Road, Cambridge CB2 1EZ, UK; fax: +44-1223-336033.

Author Contributions: The manuscript was written through contributions of all authors. E.V. and Y.O. the synthesis and characterization of the ligands and complexes, and wrote the first draft; S.J.T., solved the crystal structure of compound **1**; K.T. contributed the in-situ FTIR measurements; S.J. and T.T. contributed the DFT calculations. J.L. revised the writing; The data was analyzed by the specific author who collected the corresponding data. E.V. and J.L. reviewed the work; J.L. supervised the team. All authors have read and agreed to the published version of the manuscript.

Funding: This research was funded by the U. S. Department of Energy, Office of Science, Office of Basic Energy Sciences, grant number DE-SC0019902. This research used resources of the Advanced Light Source, which is a DOE Office of Science User Facility under contract no. DE-AC02-05CH11231.

Institutional Review Board Statement: Not applicable.

Informed Consent Statement: Not applicable.

Data Availability Statement: Not applicable.

Conflicts of Interest: The authors declare no conflict of interest. The funders had no role in the design of the study; in the collection, analyses, or interpretation of data; in the writing of the manuscript, or in the decision to publish the results.

Sample Availability: Not available.

References

1. Li, J.; Wang, X.; Zhao, G.; Chen, C.; Chai, Z.; Alsaedi, A.; Hayat, T.; Wang, X. Metal-organic framework-based materials: Superior adsorbents for the capture of toxic and radioactive metal ions. *Chem. Soc. Rev.* **2018**, *47*, 2322–2356. [[CrossRef](#)] [[PubMed](#)]
2. Wang, H.; Li, J. Microporous Metal-Organic Frameworks for Adsorptive Separation of C5-C6 Alkane Isomers. *Acc. Chem. Res.* **2019**, *52*, 1968–1978. [[CrossRef](#)]
3. Adil, K.; Belmabkhout, Y.; Pillai, R.S.; Cadiau, A.; Bhatt, P.M.; Assen, A.H.; Maurin, G.; Eddaoudi, M. Gas/vapour separation using ultra-microporous metal-organic frameworks: Insights into the structure/separation relationship. *Chem. Soc. Rev.* **2017**, *46*, 3402–3430. [[CrossRef](#)] [[PubMed](#)]
4. Bao, Z.; Chang, G.; Xing, H.; Krishna, R.; Ren, Q.; Chen, B. Potential of microporous metal-organic frameworks for separation of hydrocarbon mixtures. *Energy Environ. Sci.* **2016**, *9*, 3612–3641. [[CrossRef](#)]

5. Lustig, W.P.; Mukherjee, S.; Rudd, N.D.; Desai, A.V.; Li, J.; Ghosh, S.K. Metal-organic frameworks: Functional luminescent and photonic materials for sensing applications. *Chem. Soc. Rev.* **2017**, *46*, 3242–3285. [[CrossRef](#)] [[PubMed](#)]
6. Cui, Y.; Yue, Y.; Qian, G.; Chen, B. Luminescent functional metal-organic frameworks. *Chem. Rev.* **2012**, *112*, 1126–1162. [[CrossRef](#)] [[PubMed](#)]
7. Zhang, Y.; Yuan, S.; Day, G.; Wang, X.; Yang, X.; Zhou, H.-C. Luminescent sensors based on metal-organic frameworks. *Coord. Chem. Rev.* **2018**, *354*, 28–45. [[CrossRef](#)]
8. Zhao, X.; Wang, Y.; Li, D.-S.; Bu, X.; Feng, P. Metal–Organic Frameworks for Separation. *Adv. Mater.* **2018**, *30*, 1705189. [[CrossRef](#)]
9. Zhai, Q.-G.; Bu, X.; Zhao, X.; Li, D.-S.; Feng, P. Pore Space Partition in Metal–Organic Frameworks. *Acc. Chem. Res.* **2017**, *50*, 407–417. [[CrossRef](#)] [[PubMed](#)]
10. Allendorf, M.D.; Bauer, C.A.; Bhakta, R.K.; Houk, R.J. Luminescent metal-organic frameworks. *Chem. Soc. Rev.* **2009**, *38*, 1330–1352. [[CrossRef](#)]
11. Lustig, W.P.; Li, J. Luminescent metal–organic frameworks and coordination polymers as alternative phosphors for energy efficient lighting devices. *Coord. Chem. Rev.* **2018**, *373*, 116–147. [[CrossRef](#)]
12. Zhou, X.-S.; Fan, R.-Q.; Du, X.; Hao, S.-E.; Fang, R.; Wang, P.; Xing, K.; Wang, A.N.; Yang, Y.-L.; Liu, Z.-G. Key effect of robust $\pi \cdot \cdot \pi$ stacking on AIE performance for supramolecular indium(III)–organic assemblies and application in PMMA-doped hybrid material. *Inorg. Chem. Commun.* **2018**, *90*, 39–44. [[CrossRef](#)]
13. Nagarkar, S.S.; Desai, A.V.; Ghosh, S.K. A fluorescent metal-organic framework for highly selective detection of nitro explosives in the aqueous phase. *Chem. Commun.* **2014**, *50*, 8915–8918. [[CrossRef](#)]
14. Mollick, S.; Mandal, T.N.; Jana, A.; Fajal, S.; Desai, A.V.; Ghosh, S.K. Ultrastable Luminescent Hybrid Bromide Perovskite@MOF Nanocomposites for the Degradation of Organic Pollutants in Water. *ACS Appl. Nano Mater.* **2019**, *2*, 1333–1340. [[CrossRef](#)]
15. Zhai, Z.-W.; Yang, S.-H.; Cao, M.; Li, L.-K.; Du, C.-X.; Zang, S.-Q. Rational Design of Three Two-Fold Interpenetrated Metal–Organic Frameworks: Luminescent Zn/Cd-Metal–Organic Frameworks for Detection of 2,4,6-Trinitrophenol and Nitrofurazone in the Aqueous Phase. *Cryst. Growth Des.* **2018**, *18*, 7173–7182. [[CrossRef](#)]
16. Dong, X.-Y.; Huang, H.-L.; Wang, J.-Y.; Li, H.-Y.; Zang, S.-Q. A Flexible Fluorescent SCC-MOF for Switchable Molecule Identification and Temperature Display. *Chem. Mater.* **2018**, *30*, 2160–2167. [[CrossRef](#)]
17. Hu, Z.; Deibert, B.J.; Li, J. Luminescent metal-organic frameworks for chemical sensing and explosive detection. *Chem. Soc. Rev.* **2014**, *43*, 5815–5840. [[CrossRef](#)]
18. Gargurevich, I.A. Hydrogen Sulfide Combustion: Relevant Issues under Claus Furnace Conditions. *Ind. Eng. Chem. Res.* **2005**, *44*, 7706–7729. [[CrossRef](#)]
19. Meng, X.; de Jong, W.; Pal, R.; Verkooijen, A.H.M. In bed and downstream hot gas desulphurization during solid fuel gasification: A review. *Fuel Process. Technol.* **2010**, *91*, 964–981. [[CrossRef](#)]
20. Glarborg, P.; Halaburt, B.; Marshall, P.; Guillory, A.; Troe, J.; Thellefsen, M.; Christensen, K. Oxidation of reduced sulfur species: Carbon disulfide. *J. Phys. Chem. A* **2014**, *118*, 6798–6809. [[CrossRef](#)]
21. Anstey, M.; Sun, A.; Paap, S.M.; Foltz, G.; Jaeger, C.; Hoette, T.; Ochs, M.E. *Inherently Safer Technology Gaps Analysis Study*; United States. Department of Energy: Washington, DC, USA, 2012.
22. Wayne, D.; Monnery, W.Y.S.; Behie, L.A. Modelling the modified claus process reaction furnace and the implications on plant design and recovery. *Can. J. Chem. Eng.* **1993**, *71*, 711–724.
23. McGuirk, C.M.; Siegelman, R.L.; Drisdell, W.S.; Runcevski, T.; Milner, P.J.; Oktawiec, J.; Wan, L.F.; Su, G.M.; Jiang, H.Z.H.; Reed, D.A.; et al. Cooperative adsorption of carbon disulfide in diamine-appended metal-organic frameworks. *Nat. Commun.* **2018**, *9*, 5133. [[CrossRef](#)]
24. Wu, Z.-F.; Tan, B.; Feng, M.-L.; Lan, A.-J.; Huang, X.-Y. A magnesium MOF as a sensitive fluorescence sensor for CS₂ and nitroaromatic compounds. *J. Mater. Chem. A* **2014**, *2*, 6426–6431. [[CrossRef](#)]
25. Dong, Y. Tetranuclear cluster-based Pb(II)-MOF: Synthesis, crystal structure and luminescence sensing for CS₂. *J. Mol. Struct.* **2018**, *1160*, 46–49. [[CrossRef](#)]
26. Wu, Z.-F.; Tan, B.; Feng, M.-L.; Du, C.-F.; Huang, X.-Y. A magnesium-carboxylate framework showing luminescent sensing for CS₂ and nitroaromatic compounds. *J. Solid State Chem.* **2015**, *223*, 59–64. [[CrossRef](#)]
27. Wu, Z.-F.; Tan, B.; Velasco, E.; Wang, H.; Shen, N.-N.; Gao, Y.-J.; Zhang, X.; Zhu, K.; Zhang, G.-Y.; Liu, Y.-Y.; et al. Fluorescent In based MOFs showing “turn on” luminescence towards thiols and acting as a ratiometric fluorescence thermometer. *J. Mater. Chem. C* **2019**, *7*, 3049–3055. [[CrossRef](#)]
28. Wei, Z.; Gu, Z.Y.; Arvapally, R.K.; Chen, Y.P.; McDougald, R.N., Jr.; Ivy, J.F.; Yakovenko, A.A.; Feng, D.; Omary, M.A.; Zhou, H.C. Rigidifying fluorescent linkers by metal-organic framework formation for fluorescence blue shift and quantum yield enhancement. *J. Am. Chem. Soc.* **2014**, *136*, 8269–8276. [[CrossRef](#)] [[PubMed](#)]
29. Lustig, W.P.; Wang, F.; Teat, S.J.; Hu, Z.; Gong, Q.; Li, J. Chromophore-Based Luminescent Metal–Organic Frameworks as Lighting Phosphors. *Inorg. Chem.* **2016**, *55*, 7250–7256. [[CrossRef](#)]
30. Kresse, G.; Furthmüller, J. Efficient iterative schemes for \textit{ab initio} total-energy calculations using a plane-wave basis set. *Phys. Rev. B* **1996**, *54*, 11169–11186. [[CrossRef](#)] [[PubMed](#)]
31. Kresse, G.; Joubert, D. From ultrasoft pseudopotentials to the projector augmented-wave method. *Phys. Rev. B* **1999**, *59*, 1758–1775. [[CrossRef](#)]

32. Thonhauser, T.; Cooper, V.R.; Li, S.; Puzder, A.; Hyldgaard, P.; Langreth, D.C. Van der Waals density functional: Self-consistent potential and the nature of the van der Waals bond. *Phys. Rev. B* **2007**, *76*, 125112. [[CrossRef](#)]
33. Langreth, D.C.; Lundqvist, B.I.; Chakarova-Käck, S.D.; Cooper, V.R.; Dion, M.; Hyldgaard, P.; Kelkkanen, A.; Kleis, J.; Lingzhu, K.; Shen, L.; et al. A density functional for sparse matter. *J. Phys. Condens. Matter* **2009**, *21*, 084203. [[CrossRef](#)]
34. Kristian, B.; Valentino, R.C.; Kyuho, L.; Elsebeth, S.; Thonhauser, T.; Per, H.; Bengt, I.L. van der Waals forces in density functional theory: A review of the vdW-DF method. *Rep. Prog. Phys.* **2015**, *78*, 066501.
35. Chen, C.-X.; Wei, Z.-W.; Cao, C.-C.; Yin, S.-Y.; Qiu, Q.-F.; Zhu, N.-X.; Xiong, Y.-Y.; Jiang, J.-J.; Pan, M.; Su, C.-Y. All Roads Lead to Rome: Tuning the Luminescence of a Breathing Catenated Zr-MOF by Programmable Multiplexing Pathways. *Chem. Mater.* **2019**, *31*, 5550–5557. [[CrossRef](#)]
36. Hu, Z.; Huang, G.; Lustig, W.P.; Wang, F.; Wang, H.; Teat, S.J.; Banerjee, D.; Zhang, D.; Li, J. Achieving exceptionally high luminescence quantum efficiency by immobilizing an AIE molecular chromophore into a metal-organic framework. *Chem. Commun.* **2015**, *51*, 3045–3048. [[CrossRef](#)] [[PubMed](#)]
37. Wang, F.; Liu, W.; Teat, S.J.; Xu, F.; Wang, H.; Wang, X.; An, L.; Li, J. Chromophore-immobilized luminescent metal-organic frameworks as potential lighting phosphors and chemical sensors. *Chem. Commun. (Camb.)* **2016**, *52*, 10249–10252. [[CrossRef](#)]
38. Gong, Q.; Hu, Z.; Deibert, B.J.; Emge, T.J.; Teat, S.J.; Banerjee, D.; Mussman, B.; Rudd, N.D.; Li, J. Solution processable MOF yellow phosphor with exceptionally high quantum efficiency. *J. Am. Chem. Soc.* **2014**, *136*, 16724–16727. [[CrossRef](#)] [[PubMed](#)]
39. Ma, J.; Kalenak, A.P.; Wong-Foy, A.G.; Matzger, A.J. Rapid Guest Exchange and Ultra-Low Surface Tension Solvents Optimize Metal-Organic Framework Activation. *Angew. Chem. Int. Ed. Engl.* **2017**, *56*, 14618–14621. [[CrossRef](#)] [[PubMed](#)]
40. Hu, Z.; Tan, K.; Lustig, W.P.; Wang, H.; Zhao, Y.; Zheng, C.; Banerjee, D.; Emge, T.J.; Chabal, Y.J.; Li, J. Effective sensing of RDX via instant and selective detection of ketone vapors. *Chem. Sci.* **2014**, *5*, 4873–4877. [[CrossRef](#)]
41. Pramanik, S.; Hu, Z.; Zhang, X.; Zheng, C.; Kelly, S.; Li, J. A Systematic Study of Fluorescence-Based Detection of Nitroexplosives and Other Aromatics in the Vapor Phase by Microporous Metal–Organic Frameworks. *Chem. A Eur. J.* **2013**, *19*, 15964–15971. [[CrossRef](#)]
42. Hu, Z.; Lustig, W.P.; Zhang, J.; Zheng, C.; Wang, H.; Teat, S.J.; Gong, Q.; Rudd, N.D.; Li, J. Effective Detection of Mycotoxins by a Highly Luminescent Metal–Organic Framework. *J. Am. Chem. Soc.* **2015**, *137*, 16209–16215. [[CrossRef](#)] [[PubMed](#)]
43. Pramanik, S.; Zheng, C.; Zhang, X.; Emge, T.J.; Li, J. New Microporous Metal–Organic Framework Demonstrating Unique Selectivity for Detection of High Explosives and Aromatic Compounds. *J. Am. Chem. Soc.* **2011**, *133*, 4153–4155. [[CrossRef](#)] [[PubMed](#)]
44. Lustig, W.P.; Shen, Z.; Teat, S.J.; Javed, N.; Velasco, E.; O’Carroll, D.M.; Li, J. Rational design of a high-efficiency, multivariate metal–organic framework phosphor for white LED bulbs. *Chem. Sci.* **2020**, *11*, 1814–1824. [[CrossRef](#)]
45. Pang, J.; Yuan, S.; Qin, J.; Liu, C.; Lollar, C.; Wu, M.; Yuan, D.; Zhou, H.-C.; Hong, M. Control the Structure of Zr-Tetracarboxylate Frameworks through Steric Tuning. *J. Am. Chem. Soc.* **2017**, *139*, 16939–16945. [[CrossRef](#)]
46. Grissom, T.G.; Driscoll, D.M.; Troya, D.; Sapienza, N.S.; Usov, P.M.; Morris, A.J.; Morris, J.R. Molecular-Level Insight into CO₂ Adsorption on the Zirconium-Based Metal–Organic Framework, UiO-66: A Combined Spectroscopic and Computational Approach. *J. Phys. Chem. C* **2019**, *123*, 13731–13738. [[CrossRef](#)]
47. Tan, K.; Jensen, S.; Feng, L.; Wang, H.; Yuan, S.; Ferreri, M.; Klesko, J.P.; Rahman, R.; Cure, J.; Li, J.; et al. Reactivity of Atomic Layer Deposition Precursors with OH/H₂O-Containing Metal Organic Framework Materials. *Chem. Mater.* **2019**, *31*, 2286–2295. [[CrossRef](#)]
48. Mivehvar, F.; Lauzin, C.; McKellar, A.R.W.; Moazzen-Ahmadi, N. Infrared spectra of rare gas–carbon disulfide complexes: He–CS₂, Ne–CS₂, and Ar–CS₂. *J. Mol. Spectrosc.* **2012**, *281*, 24–27. [[CrossRef](#)]